Biophysical Journal
Article

Biophysical Society

Protein-induced membrane curvature in coarse-grained simulations

Taraknath Mandal,[1,5] Saverio E. Spagnolie,[2] Anjon Audhya,[3] and Qiang Cui[4,*]
[1]Department of Chemistry, Boston University, Boston, Massachusetts; [2]Department of Mathematics, University of Wisconsin-Madison, Madison, Wisconsin; [3]Department of Biomolecular Chemistry, University of Wisconsin-Madison, Madison, Wisconsin; [4]Departments of Chemistry, Physics, and Biomedical Engineering, Boston University, Boston, Massachusetts; and [5]Department of Physics, Indian Institute of Technology Kanpur, Kanpur 208016, India

ABSTRACT Using the endosomal sorting complex required for transport (ESCRT)-III membrane remodeling complex as an example, we analyze three popular coarse-grained models (the regular MARTINI, polarizable MARTINI (POL-MARTINI), and big multipole water MARTINI (BMW-MARTINI)) for the description of membrane curvature sensing and generation activities of peripheral proteins. Although the three variants of the MARTINI model provide consistent descriptions for the protein-protein interface in a linear filament model of ESCRT-III, they differ considerably in terms of protein-membrane interface and therefore membrane curvature sensing and generation behaviors. In particular, BMW-MARTINI provides the most consistent description of the protein-membrane interface as compared to all-atom simulations, whereas the regular MARTINI is most consistent with atomistic simulations in terms of the qualitative sign of membrane curvature sensing and generation. With POL-MARTINI, the ESCRT-III model interacts weakly with the membrane and therefore does not exhibit any curvature-sensitive activities. Analysis suggests that the incorrect membrane curvature activities predicted by BMW-MARTINI are due to overestimated insertion depth of an amphipathic helix and incorrect sign for the spontaneous curvature of anionic lipids. These results not only point to ways that coarse-grained models can be improved but also explicitly highlight local lipid composition and insertion depth of protein motifs as essential regulatory factors for membrane curvature sensing and generation.

SIGNIFICANCE Coarse-grained models are important to the analysis of membrane curvature sensing and generation by proteins because of the relevant length- and timescales. Factors that dictate the reliability of their predictions, however, remain unclear. Using all-atom simulations for an ESCRT-III trimer model as reference, we show that all three variants of the popular MARTINI model have limitations that impact their quantitative prediction of membrane curvature sensing and generation. An important mechanistic implication of these observations is that by modulating local lipid composition and insertion depth of protein motifs, it is possible to qualitatively change the sign for membrane curvature sensing and generation by the same protein, leading to plasticity and regulation of membrane activity of peripheral proteins.

INTRODUCTION

Cell membranes adopt various shapes in different organelles, with striking examples that include the membranes of endoplasmic reticulum (ER), the Golgi apparatus, and mitochondria (1,2). In addition, membrane shape is remodeled in various processes such as endocytosis, virus infection, cell division, and organelle biogenesis (3–8). To generate and modulate these unusual shapes and transformations of membranes, various proteins have been identified and shown to function through a range of mechanisms (9–12) that include asymmetric insertion into the bilayer, morphing membrane topology according to protein shape, lipid modifications, and crowding effects. A recent addition involves liquid-liquid phase separation of proteins on the surface of the membrane (13), leading to a local mismatch of mechanical properties and therefore inward invagination of the membrane.

Despite progress in the general mechanistic understanding of membrane curvature generation and remodeling, the situation is often not clear for a specific system because of the potential contributions from multiple mechanisms. This is the case for understanding the mechanism in vivo, which typically implicates multiple proteins that function

Submitted December 31, 2020, and accepted for publication May 28, 2021.
*Correspondence: qiangcui@bu.edu
Editor: Chris Chipot.
https://doi.org/10.1016/j.bpj.2021.05.029

together to regulate the membrane remodeling process. To tease apart the roles of specific proteins and the interdependence of the relevant components, including the contributions of specific lipids, computational studies can provide valuable insights that complement experimental investigations. Because of the large length and long timescales of membrane remodeling processes, it is often necessary to integrate computations of different scales. For example, atomistic simulations are most effective at probing local protein-membrane interactions (14,15) and perturbations in the local lipid organization that might ultimately lead to membrane curvature generation or even pore formation. To explicitly probe membrane curvature or pore formation, coarse-grained models (16,17), either particle or continuum mechanics-based ones, are usually required. This naturally leads to the question of whether predictions from coarse-grained simulations are robust, i.e., to what degree the qualitative features of curvature generation are sensitive to the details of the coarse-grained model.

On one hand, one might argue that the underlying physical mechanisms of curvature generation implicate mainly coarse features such as lipid packing, protein shape, and conformational entropy associated with disordered protein motifs. The qualitative features should be adequately captured by simple physical models and thus ought to be robust . Indeed, mechanistic insights have been gleaned for several membrane remodeling problems using elegantly simple models that employ a small number of beads to represent the proteins and lipids (18–20). On the other hand, to make the model system specific, it is likely that care is needed to reliably describe the protein-membrane interface, insertion depth of specific protein motifs, and response of lipid packing to the insertion.

In this study, we compare the membrane curvature generation behaviors predicted by three variants of the popular MARTINI model (21) (regular MARTINI (22), POL-MARTINI (23), and BMW-MARTINI (24,25)) using an oligomeric model of the endosomal sorting complex required for transport-III (ESCRT-III) complex (26) as an example. The latter is chosen because we recently conducted extensive atomistic simulations to characterize the local protein-membrane interactions (27); a membrane ribbon protocol (28) was used to explicitly demonstrate the positive local membrane curvature induced by the insertion of the N-terminal amphipathic helix. Using these atomistic results as reference, we find that all three coarse-grained models suffer from limitations that impact their ability to faithfully describe the membrane curvature generation activity of ESCRT-III. The differences in the three models, in fact, help highlight the contributions of various factors to the sign and magnitude of generated membrane curvature. All in all, the regular MARTINI model appears to generate the sign of membrane curvature most consistent with the atomistic model. Therefore, we also include its application to further test our previous hypothesis (27) that whereas ESCRT-III generates local positive curvature, the area enclosed by ESCRT-III filaments develops a negative mean curvature; the combination of these two effects and the intrinsic twist of the ESCRT-III filament (20,27,29) can lead to the initiation of the three-dimensional dome-like structure that ultimately develops into the spherical intraluminal vesicle.

MATERIALS AND METHODS

The atomistic model of the protein monomer (Fig. 1 *c*) is based on the crystal structure determined by Tang et al. (Protein Data Bank: 5FD7) (30) for the *Drosophila* ESCRT-III subunit, Snf7, at a resolution of 1.6 Å without the autoinhibitory C-terminal tail. The coordinates of the α_0 helix and those for residues 12–18 and 141–150 are missing in the crystal structure; thus, they are generated using a homology model as in our previous study (27). The coarse-grained model (Fig. 1 *d*) of the protein monomer is then generated from the atomistic model using the martinize.py script supplied by the MARTINI website. An extra elastic network is used to apply harmonic restraints between nonbonded beads based on a distance-based cutoff, with the lower and upper elastic bond cutoffs set to 0.5 and 0.9 nm, respectively, to include nonbonded beads that fall in the range of the first and second neighboring shells; the elastic bond force constant is taken to be 500 kJ $\cdot$ mol^{-1} $\cdot$ nm^{-2}. To investigate the effect of structural flexibility on protein-induced membrane curvature, we also perform simulations without any elastic network, and the results are generally similar (vide infra).

For the analysis of protein-protein interfaces, first a one-dimensional protein filament (Fig. S1) containing six monomers is built using the crystal structure lattice parameters (30). The protein filament is placed at the center of the simulation box and then solvated using different coarse-grained water models. For the regular MARTINI model (22), 10% antifreezing particles is added to avoid unphysical freezing of water. Each protein monomer has a total charge of +1 unit; thus, Cl^- ions are added to achieve overall charge neutrality. Additionally, appropriate numbers of Na^+ and Cl^- ions are added to maintain the physiological salt concentration of 150 mM. Periodic boundary conditions are enforced along all three principal directions. For

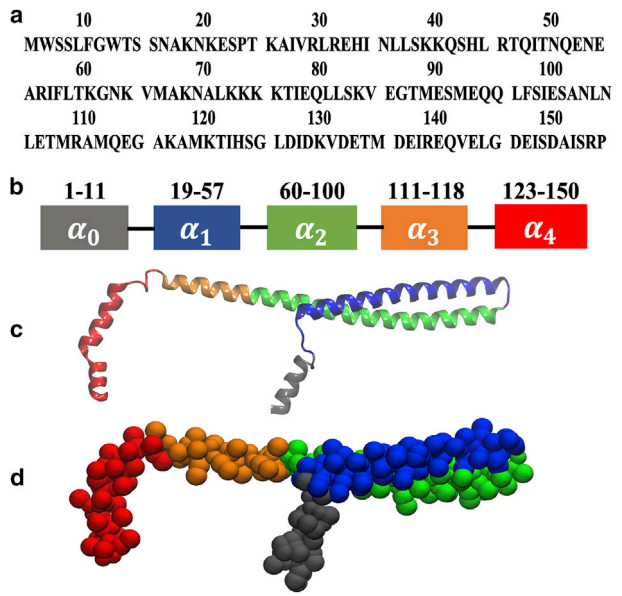

FIGURE 1 (*a*) The amino acid sequence and (*b*) the number of residues in different helices of the Snf7 protein. (*c*) The atomistic structure of the protein monomer with ribbon representation and (*d*) the coarse-grained (MARTINI) version of the protein monomer with van der Waals representation. To see this figure in color, go online.

the regular MARTINI model, the reaction-field method with a dielectric constant of 15 is used to compute electrostatic interactions, and a 1.2 nm cutoff is used for computing the van der Waals interactions. The particle mesh Ewald method (31) with a dielectric constant of 2.5 is used for electrostatic interactions in the POL-MARTINI model (23), and a 1.2 nm cutoff is also used for the van der Waals interactions. For the BMW-MARTINI model (24,25), the particle mesh Ewald method with a dielectric constant of 1.3 is used for electrostatic interactions and a 1.4 nm cutoff for van der Waals interactions. The solvated system is first energy minimized using conjugate gradient to remove any bad contacts between the solute and solvent beads; this is followed by a short NVT equilibration of 500 ps. The NVT-equilibrated system is then subject to NPT equilibration for 1 μs at 303 K and the atmospheric pressure. The temperature and pressure of the system during equilibration are controlled using a velocity rescale thermostat (32) with a time constant of 1 ps and a Parrinello-Rahman babostat (33) with a time constant of 5 ps, respectively. A time step of 10 fs is used for integrating the equations of motion. All simulations are performed using the GROMACS simulation package (34).

To study the protein-membrane interface, an Snf7 trimer is placed at ~1.5 nm (Fig. S3) from the top of a mixed lipid bilayer composed of 70% zwitterionic 1-palmitoyl-2-oleoyl-sn-glycero-3-phosphocholine (POPC) and 30% anionic 1-palmitoyl-2-oleoyl-glycero-3-phosphoserine (POPS) lipids built using CHARMM-GUI (35). The trimer is orientated such that the α_2 and α_3 helices are closer to the membrane surface because they present the most stable membrane interface in our previous all-atom study (27). With the coarse-grained models, we note that the C_{18} tails of the POPC and POPS lipids are represented by five beads in the BMW-MARTINI model, unlike the regular MARTINI or POL-MARTINI model in which these tails are represented by four beads; the extra bead does not alter the thickness or area per lipid of the bilayer (25). The protein-membrane complex is then solvated, and Na^+ ions are added to balance the negative charge of the PS lipids. Additional Na^+ and Cl^- ions are added to maintain the physiological salt concentration of 150 mM. The entire system is then equilibrated following the protocol mentioned above. To investigate the effect of insertion depth of the α_0 helices on the protein-induced membrane curvature with the BMW-MARTINI model (see below in Interplay of membrane insertion and monolayer spontaneous curvature), a harmonic potential is applied on individual α_0 helices so the center of each α_0 helix approximately coincides with the center of the top PO_4 beads of the bilayer.

To investigate the curvature sensing ability of proteins, we place an Snf7 trimer at the highest or lowest curved region of a buckled lipid bilayer. To build a buckled bilayer, we first equilibrate a membrane patch composed of 70% POPC and 30% POPS lipids. A force is then gradually applied on the equilibrated membrane along the X direction until the membrane patch adopts a sinusoidal shape. This step is followed by a further equilibration during which the X and Y lengths of the simulation box are held fixed so that the membrane patch maintains the buckled shape. After removing water and ions from this simulation box, the protein trimer is placed at the highest or lowest curved region of the buckled membrane; the system is then solvated, and ions are added to maintain 150 mM concentration as before. The entire system is then equilibrated, keeping the X and Y lengths of the simulation fixed but allowing fluctuations in the Z dimension. During production simulations, the protein trimer gradually moves to the preferred region of the buckled membrane; the speed of the movement, however, varies substantially among the different models (vide infra).

As part of the analysis, we also compare the spontaneous curvature of the lipid monolayer (C_0) computed using different models. As discussed extensively in the literature (36), C_0 is related to the first moment of the lateral pressure profile (F) as $F = -C_0K_c = -\int_0^\infty z[p_T(z) - p_N(z)]dz$, in which K_c is the monolayer bending modulus and $p_T(z)$ and $p_N(z)$ are the tangential and normal local pressures, respectively. A membrane bilayer patch is first equilibrated using either regular MARTINI or BMW-MARTINI model for coarse-grained simulations and using the CHARMM36 force field (37) for atomistic simulations. The local pressure profiles are calculated using the GROMACS-LS module developed by Vanegas et al. (38). The lateral pressure profiles are calculated for individual leaflets, which are then averaged for calculating the force in the range from 0 to ∞. The membranes bending moduli are taken from literature (39). The radius of curvature (R_0) of the monolayer is related to the monolayer spontaneous curvature (C_0) as $R_0 = C_0^{-1}$.

RESULTS AND DISCUSSION

Protein-protein interface in filament assembly

Because the ESCRT-III complex interacts with the membrane in the form of a protein filament, we first examine the stability of the protein-protein interface in a filament model in solution with various coarse-grained models. As shown in Fig. 2, *a–c*, all three coarse-grained models studied in this work capture the stability of the one-dimensional filament as observed in the atomistic simulations (27). Because the elastic network model is used in these MARTINI simulations to restrain only the structure of the protein monomers, the observation suggests that the MARTINI models adequately describe protein-protein interactions in the Snf7 filament.

To further scrutinize the protein-protein interaction sampled by the three coarse-grained models, we calculate the interhelix distances between neighboring monomers and compare the results with those obtained from previous atomistic simulations (27). Figs. 2 *e* and S2 show that the distances between each pair of the neighboring α_1, α_2, and α_3 helices are close to 3.0 nm, suggesting that the rigid core of the filament is maintained in all three coarse-grained models. The atomistic and all three coarse-grained models predict that the α_4 helix is flexible and randomly binds with the neighboring α_4 helices during the course of the simulation; as a result, the distances between neighboring α_4 helices vary significantly between 1 and 7 nm (Figs. 2 *e* and S2). The α_0 helices orient freely without any significant binding with other motifs; this is consistent with the expectation that they insert into the membrane (vide infra).

Previous atomistic simulations (27) revealed that the filament is stabilized by the interactions among the neighboring α_1, α_2, and α_3 helices through both hydrophobic and electrostatic contacts (Fig. 2 *f*). The hydrophobic residues Met87, Ile94, Ala97, Leu101, and Met104 of α_2 bind with the hydrophobic residues Met107, Met114, Ile117, and Leu121 of α_3 of the neighboring monomer, and positively charged residues Lys21, Arg25, Lys36 of α_1 and Lys69 of α_2 interact with the negatively charged residues Glu85, Glu88, Glu95, Glu102, and Glu109 of α_2 of the neighboring monomer. These hydrophobic and electrostatic interactions are also featured in the coarse-grained models; this is illustrated in Fig. 2 *f* using the regular MARTINI model as an example.

Membrane-protein interface

As discussed above, all three coarse-grained models capture filament stability as well as the correct protein-protein

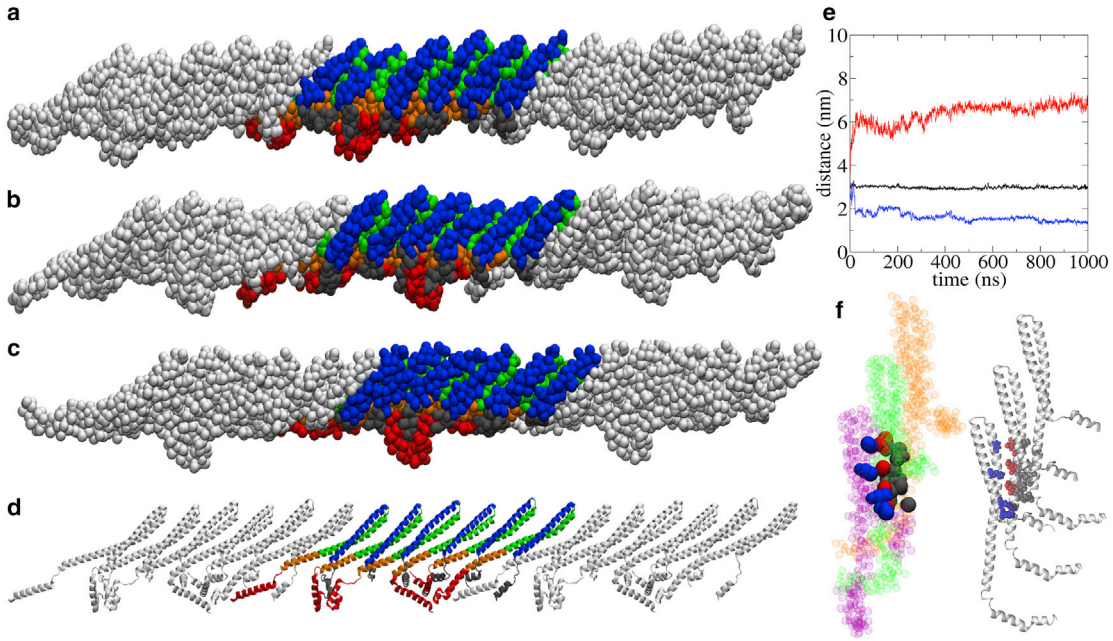

FIGURE 2 Equilibrated structures of one-dimensional Snf7 filament, which contains six protein monomers and is periodic along the *X* direction sampled from (*a*) regular MARTINI, (*b*) Pol-MARTINI, (*c*) BMW-MARTINI, and (*d*) atomistic (27) models. (*e*) Examples of typical distances between two neighboring α_4 helices (*red*, larger; *blue*, smaller) and the distance between two neighboring α_1 helices (*black*) as functions of simulation time. See text for details. Figure is shown for the regular MARTINI model only, and the other two coarse-grained models have similar features. (*f*) Hydrophobic and electrostatic interactions between neighboring monomers (see text for details) shown for (*left*) regular MARTINI model and (*right*) all-atom model. Gray, red, and blue represent the hydrophobic, negatively charged, and positively charged residues, respectively. To see this figure in color, go online.

interface in the filament. However, the protein-membrane interfaces sampled from these coarse-grained simulations are strikingly different from each other (Fig. 3, *a–c*), and in some cases, the interface differs from the atomistic predictions (Fig. 3 *d*). All-atom simulations predicted that the elongated α_2 and α_3 helices form the preferred membrane-binding interface; this is consistent with the experimental findings of Buchkovich et al. (40) that mutation of lysine residues in this interface to negatively charged residues significantly decreased the membrane-binding activity of the Snf7 filament, whereas mutations of cationic residues on α_1 had a negligible impact. This feature is only captured by BMW-MARTINI, in which the α_2 and α_3 helices are readily adsorbed on the membrane surface. By contrast, with the regular MARTINI and POL-MARTINI, the Snf7 trimer is not well adsorbed on the membrane surface and adopts a tilted configuration with respect to the membrane interface (Figs. 3, *a* and *b*, and 4). For example, as shown in Fig. 4, the numbers of close protein-membrane contacts (within 0.6 nm) with the regular MARTINI and POL-MARTINI models are substantially lower than those for BMW-MARTINI. More specifically, the experimental results of Buchkovich et al. (40) pointed to the following lysine residues in the α_2 and α_3 helices as implicated in membrane binding: Lys60, Lys64, Lys68, Lys71, Lys79, Lys112, and Lys115. Although these lysine residues reside at the protein-membrane interface predicted by the atomistic and BMW-MARTINI models (Fig. 3, *f* and *g*), the regular MARTINI (Fig. 3 *e*) and POL-MARTINI models sample those lysine residues far from the membrane surface, clearly indicating that they fail to capture the correct protein-membrane interface.

The α_0 helix is also essential to the membrane-binding activity of the Snf7 protein as suggested by experimental studies; deletion of the N-terminal helix completely abolished the ability of Snf7 to bind with the membrane (40). Fig. S4 shows that with the BMW-MARTINI model, all three α_0 helices are deeply inserted inside the membrane, and the insertion depth is even deeper than that in atomistic simulations (27). By contrast, the POL-MARTINI model shows that the insertion of the α_0 helices is significantly shallower; only two out of three α_0 helices remain close to the membrane surface, a result likely due to the tilted orientation of the Snf7 trimer with respect to the membrane interface. The insertion depth of the α_0 helices with the regular MARTINI model is also not as deep as the BMW-MARTINI or atomistic models, though all three α_0 helices remain close to the membrane surface.

The α_4 helix contains several negatively charged residues, including Asp127, Glu128, Asp131, Glu132, Glu135, Glu138, Asp141, Glu142, and Asp145; thus, it is not likely to bind with the anionic membrane that contains PS lipids. Only one out of three α_4 helices bind to the membrane surface during the atomistic simulations; qualitatively similar behavior is seen in the regular MARTINI simulation as well. However, in the BMW-MARTINI simulations, all

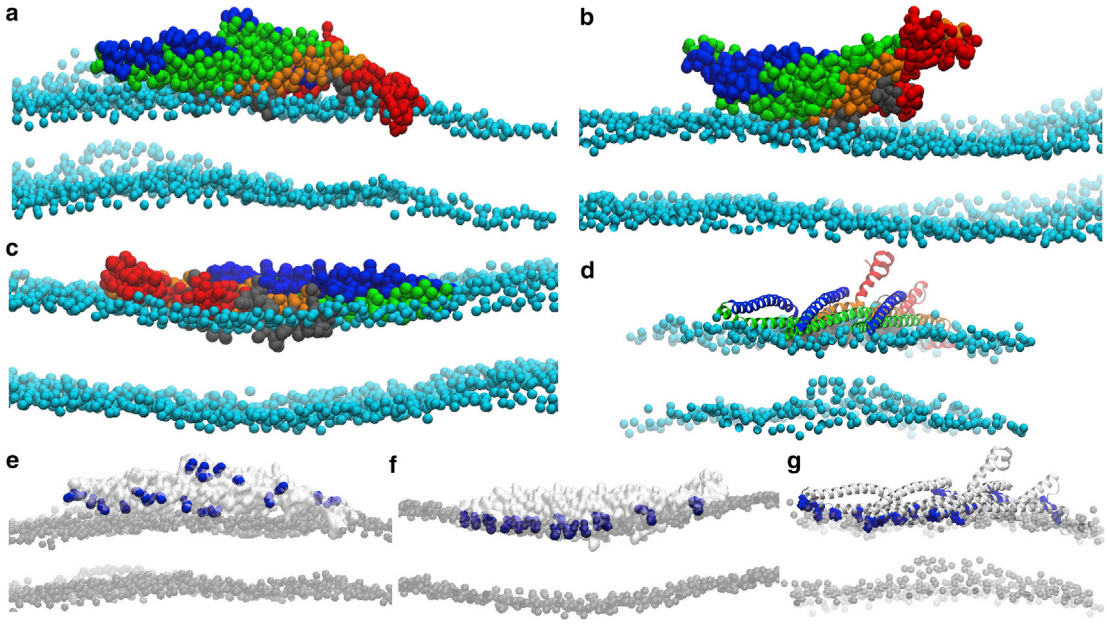

FIGURE 3 Equilibrated structures of the protein-membrane interface sampled by (*a*) regular MARTINI, (*b*) POL-MARTINI, (*c*) BMW-MARTINI, and (*d*) atomistic (27) models. Cyan color represents either PO_4 beads (coarse-grained models) or *P* atoms (atomistic model). Gray, blue, green, orange, and red colors represent the α_0, α_1, α_2, α_3, and α_4 helices, respectively. Positively charged Lys60, Lys64, Lys68, Lys71, Lys79, Lys112, and Lys115 residues located in the α_2 and α_3 helices are highlighted for the structures obtained from (*e*) regular MARTINI, (*f*) BMW-MARTINI, and (*g*) atomistic (27) simulations. To see this figure in color, go online.

three α_4 helices are strongly adsorbed on the membrane surface, suggesting a very strong protein-membrane interaction. By contrast, none of the α_4 helices are adsorbed on the membrane surface with the POL-MARTINI model, reflecting minimal interactions between the Snf7 trimer and the membrane.

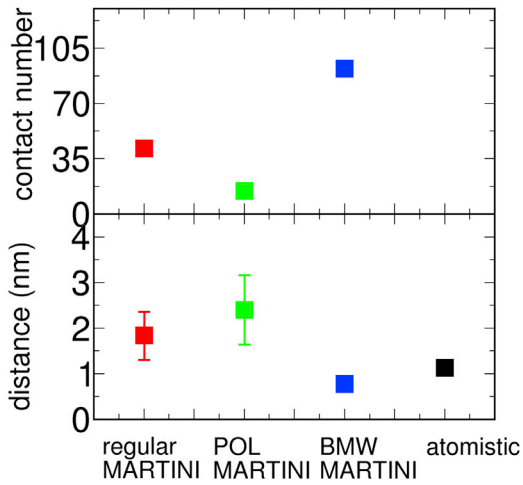

FIGURE 4 (*Top*) Total number of close contacts between the protein trimer and membrane computed from the last 1 μs trajectory of the simulation; the size of the standard deviation is comparable to the symbol size. Contacts from atomistic simulations are not listed because of the different model resolutions. (*Bottom*) The distance of the protein core (center of the α_1, α_2, and α_3 helices) from the top PO_4 (coarse-grained) or *P* atom (atomistic) layers. The mean distance is calculated by averaging the distances of the core of the three monomers (time averaged distance for individual monomer is given in Fig. S4) and the error bars are calculated from the standard deviations. To see this figure in color, go online.

The robustness of distinct protein-membrane interfaces sampled in different coarse-grained simulations is confirmed by performing another set of independent simulations (see Fig. S5). In addition, another set of simulations is conducted without the elastic network to further investigate the impact of protein structural flexibility on the protein-membrane interface. As shown in Fig. S6, the differences among the three MARTINI models remain the same, confirming that the dissimilarity in the protein-membrane interface is intrinsic to the different coarse-grained models and not affected by the elastic network.

Protein-induced membrane curvature

ESCRT-III proteins generate vesicles through formation of an intermediate invagination that requires an intricate balance of competing positive and negative membrane curvatures. In our previous study (27), we showed that insertion of the α_0 helices of Snf7 significantly bends a flat semiperiodic membrane ribbon toward the outside, suggesting that the N-terminal α_0 helices indeed generate local positive mean curvature. Because the α_0 helices are observed here to interact with the membrane differently with the three MARTINI models, it is likely that the protein-induced membrane curvatures are also different in the different simulations.

To investigate the nature of the membrane curvature generated by the protein trimer, we divide the membrane patch into

1 nm × 1 nm grids, and then the Z component of the center of mass of the PO_4 beads (coarse-grained simulations) or P atoms (atomistic simulations) of both leaflets in each grid is time averaged for the last 1 μs (coarse-grained simulations) or 50 ns (atomistic simulations) of the production run. Such membrane height data are then used to compute the mean membrane curvature shown in Fig. 5.

As shown in Figs. 5 *a* and S7 *b* (from an independent set of simulations), the Snf7 trimer generates a positive membrane curvature with the regular MARTINI model, which qualitatively agrees with the atomistic results (Fig. 5 *d*). Despite the regular MARTINI model poorly predicting the protein-membrane interface, the positive membrane curvature is generated because of the insertion of the α_0 helices into the membrane. This observation is in line with the results from our previous all-atom study (27) that curvature generation was largely dictated by the α_0 helices. By contrast, even though the BMW-MARTINI model samples the protein-membrane interface substantially closer to the atomistic result, the protein trimer induces a negative membrane curvature with this model (Figs. 5 *c* and S7 *d*). With POL-MARTINI, the protein trimer induces almost no curvature on the membrane (Figs. 5 *b* and S7 *c*) because the α_0 helices minimally interact with the membrane, as discussed above. Finally, as shown in Fig. S8, the distinct nature of the membrane curvatures from various MARTINI models remains in simulations that do not impose the elastic network model on the protein.

Membrane curvature sensing by the Snf7 trimer

A necessary, but not sufficient, condition for a protein to generate membrane curvature is to preferentially bind to a curved membrane over a flat membrane (41); if the preferential binding free energy is larger in magnitude than the membrane bending energy, curvature can be generated. To further compare the variants of MARTINI models and contrast their descriptions of protein-membrane interactions, we next compare their ability to predict the membrane curvature sensing activities of the Snf7 trimer.

With the regular MARTINI model, as shown in Fig. 6 *a* (also see Video S1), the Snf7 trimer spontaneously moves away from a negatively curved region and climbs up toward a positively curved region within 900 ns; it remains at the top for the rest of the 2.5 μs simulations. This suggests that the regular MARTINI model predicts that the Snf7 trimer prefers a positively curved region, which is consistent with the generation of positive membrane curvature observed in the previous subsection. With BMW-MARTINI, by contrast, the Snf7 trimer remains at the negatively curved region throughout the 5 μs MD simulation (Fig. S10). Moreover, when placed initially at the top of the buckled membrane, the protein trimer moves spontaneously toward the negatively curved region (Fig. 6 *c*; Video S2) during the course of 10 μs simulations. These observations suggest that the BMW-MARTINI model predicts that the Snf7 trimer prefers negative membrane curvature, again consistent with the generation

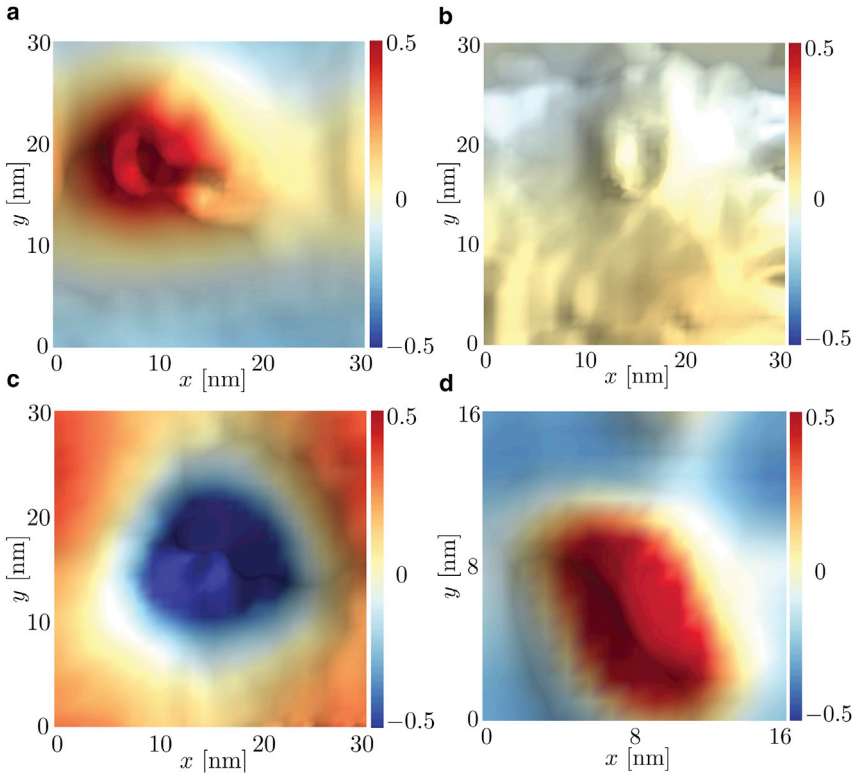

FIGURE 5 Two-dimensional plots of Snf7-trimer induced membrane curvature (in nm^{-1}) calculated from (*a*) regular MARTINI, (*b*) POL-MARTINI, (*c*) BMW-MARTINI, and (*d*) atomistic (27) simulations. See text for details. To see this figure in color, go online.

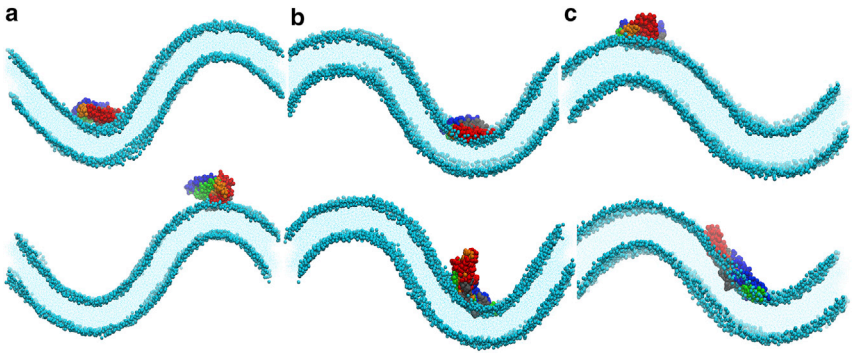

FIGURE 6 Curvature sensing by the Snf7 trimer in the buckled membrane simulations with the (*a*) regular MARTINI, (*b*) POL-MARTINI, and (*c*) BMW-MARTINI models. The initial and final locations of the Snf7 trimer are shown in the top and bottom panels, respectively. See text for details; for videos that illustrate the change of protein location during the simulations, see Supporting material. To see this figure in color, go online.

of negative membrane curvature discussed in the last subsection. With the POL-MARTINI model, when placed initially at the negatively curved region (Fig. 6 *b*, *top*), the protein trimer initially moves up slightly but then comes back to its initial position within 4 μs of simulation (Fig. 6 *b*, *bottom*). However, when the trimer is initially placed at the positively curved region of the buckled membrane, it remains there for the entire 2 μs simulation (Fig. S10). These observations suggest that with POL-MARTINI, the Snf7 trimer has no strong preference toward any curved region, likely because of its weak interaction with the membrane with this model.

Monolayer spontaneous curvature

Another potentially important property to membrane curvature generation is the monolayer spontaneous curvature C_0. Accordingly, we have compared C_0 computed using the three variants of MARTINI and atomistic model, and the results for different lipids are summarized in Fig. 7 and in Table S1. For 1,2-Dioleoyl-sn-glycero-3-phosphoethanolamine (DOPE) and 1,2-Dioleoyl-sn-glycero-3-phosphocholine (DOPC) monolayers, atomistic, BMW-MARTINI, and regular MARTINI models have comparable results that are in fair agreement with experimental values. However, for anionic lipids such as phosphatidylserine (PS) and phosphatidylglycerol (PG), BMW-MARTINI predicts a strong negative spontaneous curvature that is incorrect in sign and magnitude compared with the regular MARTINI and atomistic models. For example, BMW-MARTINI estimates the radius of curvature of the POPS monolayer to be -18 Å, whereas it is $+89$ and $+148$ Å by the regular MARTINI and atomistic model, respectively.

CONCLUSIONS

Interplay of membrane insertion and monolayer spontaneous curvature

The simulation results show that even though the protein-protein interface is correctly captured by all three coarse-grained models, the protein-membrane interface predicted by these models are significantly different from each other. These results highlight that a reliable description of electrostatics is essential to the proper description of protein-membrane interactions in coarse-grained simulations. Along this line, the BMW-MARTINI model appears most appropriate as reflected by the observation that it captures the interfacial electrostatic potential in reasonable agreement with all-atom simulations and experiment (25), in contrast to the original MARTINI and POL-MARTINI (23). This is further supported by recent analysis of cationic nanoparticle-membrane interactions by different groups (42,43).

Moreover, the protein-induced membrane curvature is also predicted inconsistently by the different MARTINI models, particularly because the α_0 helices interact with the membrane differently with these models. The amphipathic helices induce membrane curvature by changing the lipid packing and their orientation with respect to the membrane surface, as discussed extensively in other curvature generation systems such as the BAR domain (10,14) and ArfGAP1 (44). It has been proposed (45) that the sign of the generated membrane curvature depends on the chemical nature of the amphipathic helix as illustrated in Fig. 8 *a*. If the hydrophilic interactions are stronger than the hydrophobic interactions, then the hydrophilic part remains close to the membrane surface to gain access to the hydrophilic lipid heads and solvent, with the hydrophobic part inserting shallowly into the membrane to interact with the hydrophobic lipid tails. In this scenario, the proximal lipid tails change their orientation such that a positive mean curvature is formed as shown in Fig. 8 *a*, top. However, if the hydrophobic interactions are much stronger than the hydrophilic interactions, then the helix enters much deeper inside the membrane, and lipid molecules change their orientations toward a negative mean curvature, as shown in Fig. 8 *a*, bottom. Because the insertion of the α_0 helices is much deeper in the BMW-MARTINI model compared with the regular MARTINI model, the mechanism proposed in Fig. 8 *a* provides a plausible explanation for the generation and preference to distinct membrane curvatures observed in those simulations.

To further test this hypothesis, we perform a control simulation with the BMW-MARTINI model in which the α_0 helices are restrained to insert not as deeply, with an umbrella

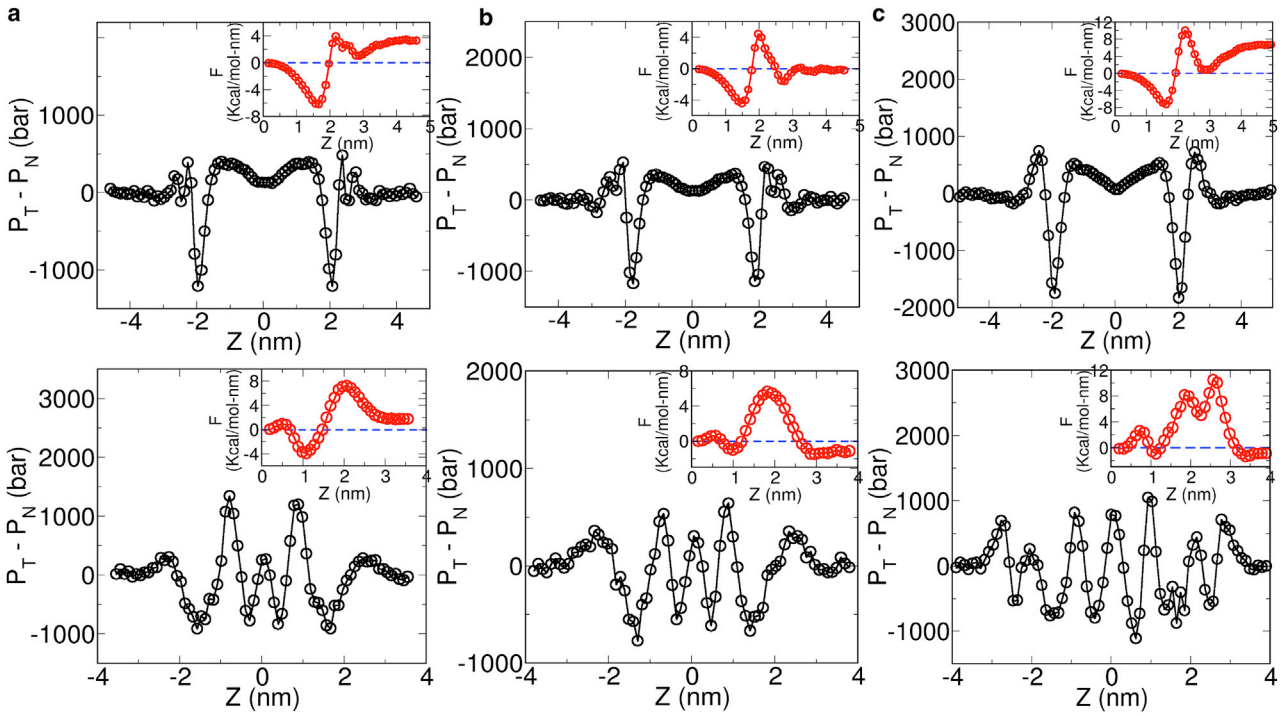

FIGURE 7 The difference between the tangential and normal local pressure as a function of the distance from the bilayer center which is located at $z = 0$; the pressure profiles are shown for (*a*) DOPE, (*b*) POPC, and (*c*) POPS bilayers. The top and bottom panels show the results obtained from the BMW-MARTINI and atomistic model, respectively. The inset in each figure shows the force corresponding to the pressure profile as a function of the distance from the bilayer center, i.e., $F = -\int_0^\infty z[p_T(z) - p_N(z)]dz$. For the decomposition of the pressure profiles, see Fig. S9. To see this figure in color, go online.

potential applied to the center of the individual α_0 helix relative to the center of the top PO_4 layer. Specifically, when the restrained insertion depth is comparable to that in the atomistic simulations, Fig. 8 *b* shows that the induced negative membrane curvature indeed decreases significantly (compare with Fig. 5 *c*). On the other hand, limiting the insertion depth of the α_0 helices does not completely abolish the negative membrane curvature formation, suggesting that other factors also contribute.

As discussed above, BMW-MARTINI also leads to incorrect spontaneous curvature for anionic lipids such as PS and PG, which might also contribute to the incorrect negative membrane curvature generation for the Snf7 trimer predicted by the BMW-MARTINI model. To confirm this, we repeat the membrane curvature simulation with the BMW-MARTINI model by changing all the POPS lipids to POPC lipids. The protein trimer (α_2 and α_3 helices) remain well adsorbed on the membrane surface, whereas the insertion depth of the α_0 helices slightly decreases compared with the POPC + POPS membrane system (Fig. 8 *d*). As shown in Fig. 8 *c*, the negative membrane curvature is substantially reduced as compared with the case with a mixed POPC/POPS bilayer (compare Figs. 5 *c* and 8 *c*). Therefore, collectively, the results in Fig. 8, *b* and *c* suggest that the incorrect negative spontaneous curvature for anionic lipids and overestimated insertion depth of the amphipathic helices combine to induce a significant negative membrane curvature by the Snf7 trimer with BMW-MARTINI.

The observation of qualitatively different membrane curvature sensing and generation behaviors with the three closely related coarse-grained models highlights that specific molecular level of detail is indeed important to the proper description of membrane remodeling activity of proteins, highlighting the importance of carefully calibrating popular coarse-grained models for specific applications. Along this line, although BMW-MARTINI generally provides an adequate description of interfacial electrostatics and therefore the protein-membrane interface, nonpolar terms in this model need to be refined to correct for the overestimated insertion depth of protein motifs into the bilayer. Regarding its incorrect spontaneous curvature for systems involving anionic lipids, we have conducted decomposition of the lateral pressure profiles into contributions from various energy terms (38) for the POPC + POPS membrane, without and with the presence of the ESCRT-III trimer. For homogeneous and zwitterionic lipid bilayers, Vanegas et al. observed that the decompositions with BMW-MARTINI best resemble the atomistic results among the tested coarse-grained models (38). The results in Fig. S9 further suggest that one major difference between BMW-MARTINI and atomistic simulations is the effect of the protein on the pressure profile in the middle region of the bilayer; the

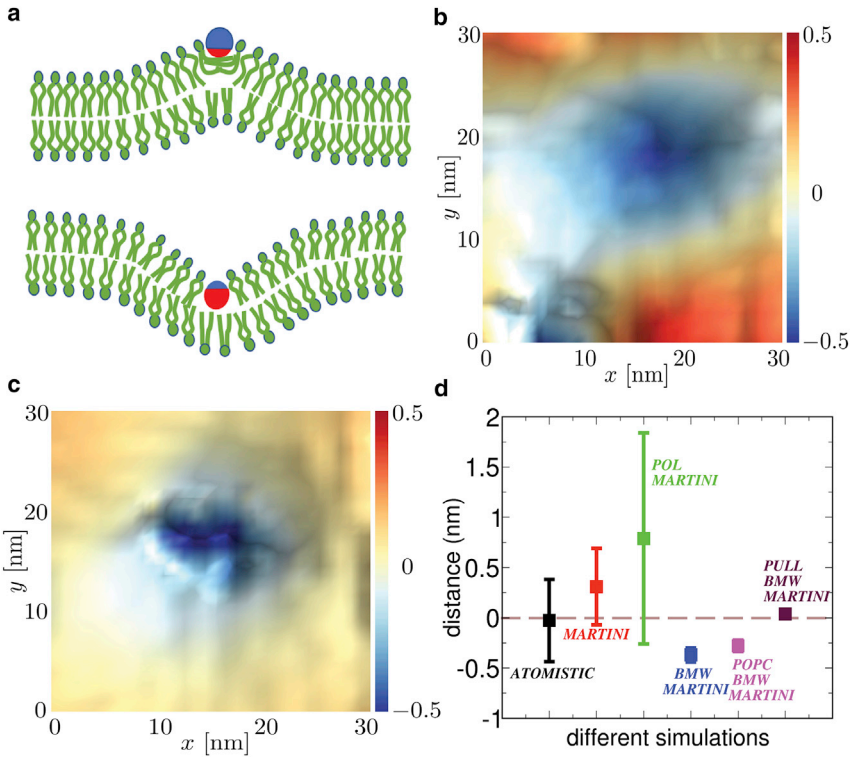

FIGURE 8 (*a*) A schematic diagram for the generation of positive (*top*) and negative (*bottom*) mean curvature by membrane insertion. The green, blue, and red colors represent the lipid, hydrophilic part of the amphipathic object, and hydrophobic part of the amphipathic object, respectively. Two-dimensional color plot of the protein-induced membrane curvature with the BMW-MARTINI model when (*b*) the individual α_0 helix is pulled up so its center is close to the top PO_4 layer and (*c*) the POPS lipids are replaced by POPC lipids. (*d*) The distance of the α_0 helix center from the center of the top layer of PO_4 bead (coarse-grained simulations) or *P* atom (atomistic simulation) in various control simulations. The mean distance is averaged over three α_0 helices and the error bars are calculated from the standard deviations; results for individual helices are shown in Fig. S4. See text for details. To see this figure in color, go online.

effect is significant at the atomistic level but almost missing at the BMW-MARTINI level, and the decomposition analysis highlights the importance of dihedral angle terms, which are missing in the coarse-grained lipid models. Therefore, to better describe spontaneous curvature and modulation of inserted protein motifs, we hypothesize that including explicit dihedral terms that better describe the anisotropic distribution of lipid tail beads is an important revision that needs to be explored systematically in future work.

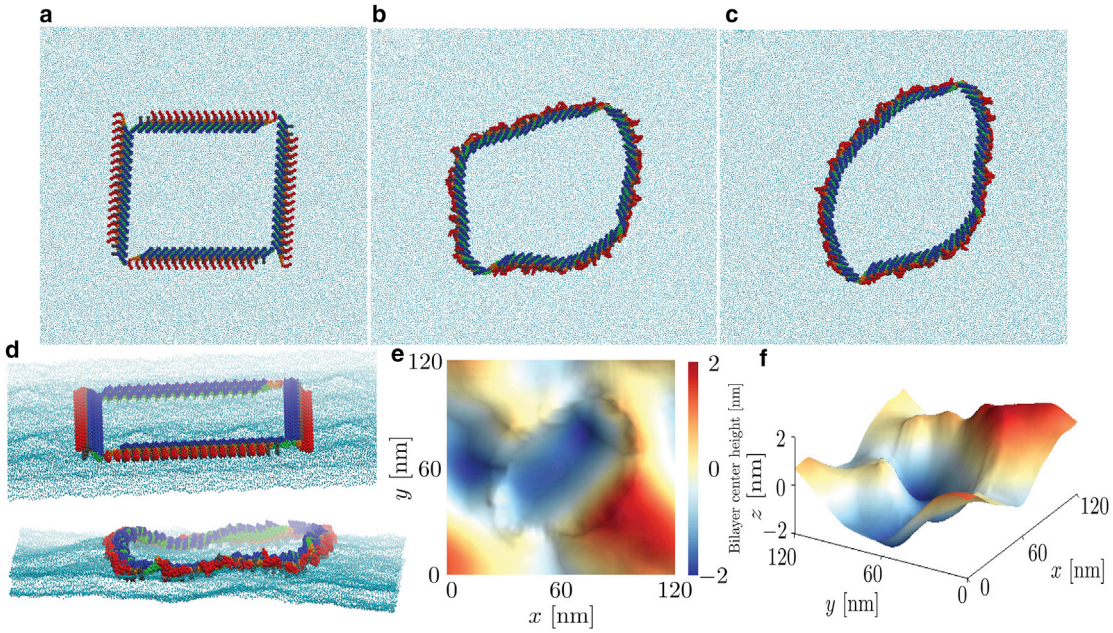

FIGURE 9 (*a*) Initial configuration of four linear protein filament placed on top of the membrane. The configuration of the protein filaments after (*b*) 500 ns and (*c*) 2.4 μs MD simulation is shown. (*d*) Side view of the protein-membrane complex at beginning (*top*) and end of 2.4 μs simulation (*bottom*). (*e*) Two- and (*f*) three-dimensional color plots of the filament induced membrane morphology. To see this figure in color, go online.

From a biological point of view, observations from this work also suggest that by modifying the lipid composition and insertion depth of protein motifs (46), it is possible to qualitatively change the sign of membrane curvature sensing and generation for the same protein; for example, the fact that deep insertion may lead to the formation of negative membrane curvature has been proposed with continuum mechanics analysis (Fig. 8; (45)), but, to the best of our knowledge, it has not been supported explicitly with experimental studies. This discussion further suggests that membrane curvature sensing and generation can be regulated by perturbing the local lipid composition and/or insertion depth via additional protein-protein interactions. The latter might explain the observation that ESCRT-III complexes, for example, appear to exhibit a considerable degree of plasticity in terms of binding to membranes with different signs of curvature (47–49). Therefore, membrane curvature sensing and generation can be particularly sensitive to the local cellular environment and context.

APPENDIX: CURVATURE GENERATION FOR MEMBRANE ENCLOSED BY CIRCULAR ESCRT-III FILAMENTS

As the ESCRT-III filament grows into a spiral, it encloses a large patch of membrane within an approximately circular area. If each ESCRT-III monomer generates a locally positive curvature due to the insertion of the α_0 helix, the combined effect of these local positive curvatures at the periphery of the circular area should induce a negative mean curvature at the center of the circular area, which, coupled with the intrinsic twist of the ESCRT-III filament (20,27,29), can develop into a three-dimensional dome structure that ultimately leads to the formation of an intraluminal vesicle. To test this hypothesis, we perform a simulation with the regular MARTINI simulation, which, as described in the main text, does not fully capture the protein-membrane interface yet does correctly predict the sign of local curvature generation. The typical sizes of the intraluminal vesicles are in the range of 10–12 nm, which requires encompassment of lipid materials of a circular area of ~50 nm diameter. Therefore, we place four linear Snf7 filaments, each of ~50 nm length (containing 17 monomers), on top of a membrane patch with a dimension of 120 nm × 120 nm (see Fig. 9 *a*); because it is not straightforward to build a circular or spiral filament, the four protein filaments are simply arranged in a rectangular shape.

Because of the large system size (~4 million beads), we have only collected 2.4 μs of simulation, which nevertheless provide valuable hints. The four linear protein filaments gradually evolve into an elliptical configuration during the course of the simulation (Fig. 9, *b* and *c*). It is remarkable to observe that protein monomers at two corners spontaneously assemble to form the expected interface as observed in a linear filament (Fig. 2); monomers at the other two corners have not established the expected interface, and further adjustments are likely needed with longer simulations. The shape of the filament fluctuates with time because of its flexibility and bilayer undulations; however, protein monomers at these two corners never detach from each other, and thus, the four filaments always encompass a certain area of the lipid membrane. Most interestingly, Fig. 9, *e* and *f* show that the elliptical (almost circular) protein filament indeed induces a significant negative curvature at the center of the circular membrane patch and positive curvature at the periphery, confirming the prediction in our previous study (27). Because the protein-membrane interface is not fully captured by the regular MARTINI model, the α_0 helices do not gain equal access to the membrane core and hence the magnitude of the positive curvature at the periphery is not uniform. We note that the protein filament interacts with its periodic images (see Fig. S11), which leads to a second negatively curved region with $X < 25$, $40 < Y < 90$.

SUPPORTING MATERIAL

Supporting material can be found online at https://doi.org/10.1016/j.bpj.2021.05.029.

AUTHOR CONTRIBUTIONS

Q.C., T.M., S.E.S., and A.A. designed the project. T.M. conducted the molecular simulations. T.M. and Q.C. analyzed the simulation data. T.M., Q.C., S.E.S., and A.A. wrote the manuscript.

ACKNOWLEDGMENTS

The work is supported by the grant National Science Foundation DMS1661900 (to A.A., Q.C., and S.E.S.). Computational resources from the Extreme Science and Engineering Discovery Environment, which is supported by National Science Foundation grant number OCI-1053575, are greatly appreciated; computations are also supported in part by the Shared Computing Cluster, which is administered by Boston University's Research Computing Services.

SUPPORTING CITATIONS

References (50–53) can be found in the Supporting material.

REFERENCES

1. Alberts, B., B. Bray, …, J. D. Watson. 1994. Molecular Biology of the Cell. Garland Publishing, Inc., New York.
2. Boal, D. 2002. Mechanics of the Cell. Cambridge University Press, Cambridge, UK.
3. McMahon, H. T., and J. L. Gallop. 2005. Membrane curvature and mechanisms of dynamic cell membrane remodelling. *Nature.* 438:590–596.
4. Lecuit, T., and F. Pilot. 2003. Developmental control of cell morphogenesis: a focus on membrane growth. *Nat. Cell Biol.* 5:103–108.
5. Marsh, M., and H. T. McMahon. 1999. The structural era of endocytosis. *Science.* 285:215–220.
6. McMahon, H. T., and I. G. Mills. 2004. COP and clathrin-coated vesicle budding: different pathways, common approaches. *Curr. Opin. Cell Biol.* 16:379–391.
7. Cho, W., and R. V. Stahelin. 2005. Membrane-protein interactions in cell signaling and membrane trafficking. *Annu. Rev. Biophys. Biomol. Struct.* 34:119–151.
8. Kirchhausen, T. 2000. Clathrin. *Annu. Rev. Biochem.* 69:699–727.
9. Bigay, J., and B. Antonny. 2012. Curvature, lipid packing, and electrostatics of membrane organelles: defining cellular territories in determining specificity. *Dev. Cell.* 23:886–895.
10. Simunovic, M., G. A. Voth, …, P. Bassereau. 2015. When physics takes over: BAR proteins and membrane curvature. *Trends Cell Biol.* 25:780–792.
11. Jarsch, I. K., F. Daste, and J. L. Gallop. 2016. Membrane curvature in cell biology: an integration of molecular mechanisms. *J. Cell Biol.* 214:375–387.
12. Zeno, W. F., K. J. Day, …, J. C. Stachowiak. 2020. Principles and applications of biological membrane organization. *Annu. Rev. Biophys.* 49:19–39.

13. Yuan, F., H. Alimohamadi, …, J. C. Stachowiak. 2021. Membrane bending by protein phase separation. *Proc. Natl. Acad. Sci. USA.* 118:e2017435118.
14. Cui, H., E. Lyman, and G. A. Voth. 2011. Mechanism of membrane curvature sensing by amphipathic helix containing proteins. *Biophys. J.* 100:1271–1279.
15. Zhang, L., M. Rajendram, …, Q. Cui. 2016. Ionic hydrogen bonds and lipid packing defects determine the binding orientation and insertion depth of RecA on multicomponent lipid bilayers. *J. Phys. Chem. B.* 120:8424–8437.
16. Simunovic, M., E. Evergren, …, P. Bassereau. 2016. How curvature-generating proteins build scaffolds on membrane nanotubes. *Proc. Natl. Acad. Sci. USA.* 113:11226–11231.
17. Bassereau, P., R. Jin, …, T. R. Weikl. 2018. The 2018 biomembrane curvature and remodeling roadmap. *J. Phys. D Appl. Phys.* 51:343001.
18. Reynwar, B. J., G. Illya, …, M. Deserno. 2007. Aggregation and vesiculation of membrane proteins by curvature-mediated interactions. *Nature.* 447:461–464.
19. Deserno, M. 2015. Fluid lipid membranes: from differential geometry to curvature stresses. *Chem. Phys. Lipids.* 185:11–45.
20. Harker-Krischneck, L., B. Baum, and A. Saric. 2019. Transitions in filament geometry drive ESCRT-III-mediated membrane remodeling and fission. *BMC Biol.* 17:82.
21. Marrink, S. J., and D. P. Tieleman. 2013. Perspective on the Martini model. *Chem. Soc. Rev.* 42:6801–6822.
22. Marrink, S. J., H. J. Risselada, …, A. H. de Vries. 2007. The MARTINI force field: coarse grained model for biomolecular simulations. *J. Phys. Chem. B.* 111:7812–7824.
23. Yesylevskyy, S. O., L. V. Schäfer, …, S. J. Marrink. 2010. Polarizable water model for the coarse-grained MARTINI force field. *PLoS Comput. Biol.* 6:e1000810.
24. Wu, Z., Q. Cui, and A. Yethiraj. 2010. A new coarse-grained model for water: the importance of electrostatic interactions. *J. Phys. Chem. B.* 114:10524–10529.
25. Wu, Z., Q. Cui, and A. Yethiraj. 2011. A new coarse-grained force field for membrane-peptide simulations. *J. Chem. Theory Comput.* 7:3793–3802.
26. Im, Y. J., T. Wollert, …, J. H. Hurley. 2009. Structure and function of the ESCRT-II-III interface in multivesicular body biogenesis. *Dev. Cell.* 17:234–243.
27. Mandal, T., W. Lough, …, Q. Cui. 2020. Molecular simulation of mechanical properties and membrane activities of the ESCRT-III complexes. *Biophys. J.* 118:1333–1343.
28. Wu, Z., and K. Schulten. 2014. Synaptotagmin's role in neurotransmitter release likely involves Ca(2+)-induced conformational transition. *Biophys. J.* 107:1156–1166.
29. Pfitzner, A. K., V. Mercier, …, A. Roux. 2020. An ESCRT-III polymerization sequence drives membrane deformation and fission. *Cell.* 182:1140–1155.e18.
30. Tang, S., W. M. Henne, …, S. D. Emr. 2015. Structural basis for activation, assembly and membrane binding of ESCRT-III Snf7 filaments. *eLife.* 4:e12548.
31. Darden, T., D. York, and L. Pedersen. 1993. Particle mesh Ewald: an N log(N) method for Ewald sums in large systems. *J. Chem. Phys.* 98:10089–10092.
32. Bussi, G., D. Donadio, and M. Parrinello. 2007. Canonical sampling through velocity rescaling. *J. Chem. Phys.* 126:014101.
33. Parrinello, M., and A. Rahman. 1981. Polymorphic transitions in single crystals: a new molecular dynamics method. *J. Appl. Phys.* 52:7182–7190.
34. Abraham, M. J., T. Murtola, …, E. Lindahl. 2015. GROMACS: high performance molecular simulations through multi-level parallelism from laptops to supercomputers. *SoftwareX.* 1–2:19–25.
35. Jo, S., T. Kim, …, W. Im. 2008. CHARMM-GUI: a web-based graphical user interface for CHARMM. *J. Comput. Chem.* 29:1859–1865.
36. Sodt, A. J., and R. W. Pastor. 2013. Bending free energy from simulation: correspondence of planar and inverse hexagonal lipid phases. *Biophys. J.* 104:2202–2211.
37. Klauda, J. B., R. M. Venable, …, R. W. Pastor. 2010. Update of the CHARMM all-atom additive force field for lipids: validation on six lipid types. *J. Phys. Chem. B.* 114:7830–7843.
38. Vanegas, J. M., A. Torres-Sánchez, and M. Arroyo. 2014. Importance of force decomposition for local stress calculations in biomembrane molecular simulations. *J. Chem. Theory Comput.* 10:691–702.
39. Venable, R. M., F. L. H. Brown, and R. W. Pastor. 2015. Mechanical properties of lipid bilayers from molecular dynamics simulation. *Chem. Phys. Lipids.* 192:60–74.
40. Buchkovich, N. J., W. M. Henne, …, S. D. Emr. 2013. Essential N-terminal insertion motif anchors the ESCRT-III filament during MVB vesicle formation. *Dev. Cell.* 27:201–214.
41. Cui, Q., L. Zhang, …, A. Yethiraj. 2013. Generation and sensing of membrane curvature: where materials science and biophysics meet. *Curr. Opin. Solid State Mater. Sci.* 17:164–174.
42. Sheavly, J. K., J. A. Pedersen, and R. C. Van Lehn. 2019. Curvature-driven adsorption of cationic nanoparticles to phase boundaries in multicomponent lipid bilayers. *Nanoscale.* 11:2767–2778.
43. Das, M., U. Dahal, …, Q. Cui. 2019. Molecular dynamics simulation of interaction between functionalized nanoparticles with lipid membranes: analysis of coarse-grained models. *J. Phys. Chem. B.* 123:10547–10561.
44. Antonny, B. 2011. Mechanisms of membrane curvature sensing. *Annu. Rev. Biochem.* 80:101–123.
45. Campelo, F., H. T. McMahon, and M. M. Kozlov. 2008. The hydrophobic insertion mechanism of membrane curvature generation by proteins. *Biophys. J.* 95:2325–2339.
46. Graham, T. R., and M. M. Kozlov. 2010. Interplay of proteins and lipids in generating membrane curvature. *Curr. Opin. Cell Biol.* 22:430–436.
47. Allison, R., J. H. Lumb, …, E. Reid. 2013. An ESCRT-spastin interaction promotes fission of recycling tubules from the endosome. *J. Cell Biol.* 202:527–543.
48. McCullough, J., A. K. Clippinger, …, A. Frost. 2015. Structure and membrane remodeling activity of ESCRT-III helical polymers. *Science.* 350:1548–1551.
49. Bertin, A., N. de Franceschi, …, P. Bassereau. 2020. Human ESCRT-III polymers assemble on positively curved membranes and induce helical membrane tube formation. *Nat. Commun.* 11:2663.
50. Leikin, S., M. M. Kozlov, …, R. P. Rand. 1996. Measured effects of diacylglycerol on structural and elastic properties of phospholipid membranes. *Biophys. J.* 71:2623–2632.
51. Doktorova, M., D. Harries, and G. Khelashvili. 2017. Determination of bending rigidity and tilt modulus of lipid membranes from real-space fluctuation analysis of molecular dynamics simulations. *Phys. Chem. Chem. Phys.* 19:16806–16818.
52. Szule, J. A., N. L. Fuller, and R. P. Rand. 2002. The effects of acyl chain length and saturation of diacylglycerols and phosphatidylcholines on membrane monolayer curvature. *Biophys. J.* 83:977–984.
53. Fuller, N., C. R. Benatti, and R. P. Rand. 2003. Curvature and bending constants for phosphatidylserine-containing membranes. *Biophys. J.* 85:1667–1674.